



**HAL**  
open science

## **Analytical study of air-gap surface force – application to electrical machines**

Raphaël Pile, Jean Le Besnerais, Guillaume Parent, Emile Devillers, Thomas Henneron, Yvonnick Le Menach, Jean-Philippe Lecointe

► **To cite this version:**

Raphaël Pile, Jean Le Besnerais, Guillaume Parent, Emile Devillers, Thomas Henneron, et al.. Analytical study of air-gap surface force – application to electrical machines. *Open Physics*, 2020, 18 (1), pp.658-673. 10.1515/phys-2020-0147 . hal-03197884

**HAL Id: hal-03197884**

**<https://univ-artois.hal.science/hal-03197884>**

Submitted on 20 Apr 2021

**HAL** is a multi-disciplinary open access archive for the deposit and dissemination of scientific research documents, whether they are published or not. The documents may come from teaching and research institutions in France or abroad, or from public or private research centers.

L'archive ouverte pluridisciplinaire **HAL**, est destinée au dépôt et à la diffusion de documents scientifiques de niveau recherche, publiés ou non, émanant des établissements d'enseignement et de recherche français ou étrangers, des laboratoires publics ou privés.

## Research Article

Raphaël Pile\*, Jean Le Besnerais, Guillaume Parent, Emile Devillers, Thomas Henneron, Yvonnick Le Menach, and Jean-Philippe Lecoïnte

# Analytical study of air-gap surface force – application to electrical machines

<https://doi.org/10.1515/phys-2020-0147>  
received April 26, 2020; accepted June 25, 2020

**Abstract:** The Maxwell stress tensor (MST) method is commonly used to accurately compute the global efforts, such as electromagnetic torque ripple and unbalanced electromagnetic forces in electrical machines. The MST has been extended to the estimation of local magnetic surface force for the vibroacoustic design of electrical machines under electromagnetic excitation. In particular, one common air-gap surface force (AGSF) method based on MST is to compute magnetic surface forces on a cylindrical shell in the air gap. However, the AGSF distribution depends on the radius of the cylindrical shell. The main contribution of this study is to demonstrate an analytic transfer law of the AGSF between the air gap and the stator bore radius. It allows us to quantify the error between the magnetic surface force calculated in the middle of the air gap and the magnetic force computed on the stator teeth. This study shows the strong influence of the transfer law on the computed tangential surface force distribution through numerical applications with induction and synchronous electrical machines. Finally, the surface force density at stator bore radius is more accurately estimated when applying the new transfer law on the AGSF.

\* **Corresponding author: Raphaël Pile**, Univ. Lille, Arts et Metiers ParisTech, Centrale Lille, HEI, EA 2697 – L2EP, Lille, France; Laboratoire d'Electrotechnique et d'Electronique de Puissance, F-59000, Lille, France; EOMYS ENGINEERING, Lille-Hellemmes, Lille, 59260, France; Univ. Artois, EA 4025, Laboratoire Systèmes Électrotechniques et Environnement (LSEE), F-62400, Béthune, France, e-mail: raphael.pile@eomys.com

**Jean Le Besnerais, Emile Devillers:** EOMYS ENGINEERING, Lille-Hellemmes, Lille, 59260, France

**Guillaume Parent, Jean-Philippe Lecoïnte:** Univ. Artois, EA 4025, Laboratoire Systèmes Électrotechniques et Environnement (LSEE), F-62400, Béthune, France

**Thomas Henneron, Yvonnick Le Menach:** Univ. Lille, Arts et Metiers ParisTech, Centrale Lille, HEI, EA 2697 – L2EP, Lille, France; Laboratoire d'Electrotechnique et d'Electronique de Puissance, F-59000, Lille, France

**Keywords:** magnetic forces, noise and vibration, Maxwell tensor, electrical machine, air gaps

## 1 Introduction

The Maxwell stress tensor (MST) method based on a closed surface is commonly used to accurately compute the electromagnetic torque and global forces in electrical machines [1–5]. The issue of local magnetic force computation has been addressed in many publications from the electromagnetic energy derivation [1,6–8] to the application of numerical methods [9–11]. However, recent developments in the field of electromagnetic vibrations for electrical machines show a preference for estimating local magnetic forces based on the MST in the air gap [12–17].

The air-gap surface force (AGSF) method based on MST consists in computing equivalent magnetic surface forces with a cylindrical shell in the middle of the air gap. The AGSF is based on the assumption that the air gap is relatively thin in electrical machines and that the difference will be negligible for vibroacoustic analysis. This study proposes to discuss these assumptions. The popularity of the methods based on AGSF is mainly due to the compatibility of the method with analytical modeling techniques as permeance and magneto-motive force [18–22]. Indeed, analytical models are able to calculate the magnetic field of the electric machine only in the middle of the air gap. Thus, only the AGSF is available to estimate magnetic excitation. Alternatively, semi-analytical methods [23,24] are able to calculate the magnetic field in the whole air-gap band. A downside of this approach is the Gibbs phenomenon [25] that reduces the accuracy of AGSF computed on the stator bore radius. The energy derivation methods are not compatible with analytical and semi-analytical methods to compute magnetic local forces as the knowledge of the magnetic field is not available everywhere in the electrical machine. As a consequence, only the AGSF method is available for analytical methods.

Nevertheless, the compatibility with analytical and semi-analytical methods allows us to perform fast vibroacoustic design, optimization and troubleshoot at low computational cost [20,21]. Indeed, the AGSF is also compatible with frequency response function (FRF) based on mechanical analytical models for vibration prediction [26,27]: thanks to an angular Fourier transform of the AGSF, the vibration response to each AGSF wavenumber can be performed. Then, the most harmful excitation can be identified. This magneto-mechanical coupling is also used with mechanical finite element analysis (FEA) because the angular wavenumber decomposition along a circular path allows us to troubleshoot the electromagnetic sources of vibrations [28].

The AGSF is used to calculate equivalent distributed forces at the neutral fiber of the stator yoke [21] or on the tip of the stator teeth [29]. Several models have recently been proposed to compute from the AGSF the equivalent forces which applies to the neutral fiber [30,31]. In some cases, the AGSF is integrated as lumped tooth forces [14,32].

The variation of AGSF as a function of radius was mainly studied numerically [33]: the AGSF position has an effect on vibration results at high frequency. This is consistent with the study [34] which shows an analytical dependency of AGSF results with radius and angular wavenumber for a theoretical slotless machine. The analytical calculation of global forces and torque – which correspond to the integral of the 0th AGSF wavenumbers – has been studied in ref. [35,36]. The analytic study of higher AGSF wavenumbers is one objective of this study.

A new analytic transfer law (45) was introduced in ref. [37], which allows us to compute the AGSF at the stator teeth tip radius – or stator bore radius – based on the AGSF in the middle of the air gap. This transfer law is a generalization of the solution proposed in ref. [34]. This transfer law allows us to understand how the magnetic force wavenumber depends on the air-gap radius of computation. It does not depend on the topology of the rotating electrical machine. The formula remains valid in the whole air-gap band, even in front of the slots. The main contribution of the study is to demonstrate the AGSF transfer law proposed in ref. [37]. This study also discusses the physical interpretation of this transfer law and its application to the vibroacoustic study of electrical machines.

The study recalls the classical application of MST for AGSF. Then the transfer law is analytically demonstrated. Finally, examples of application highlight the improvement for the vibroacoustic design of squirrel-cage induction machine (SCIM) and surface permanent magnet synchronous machine (SPMSM).

## 2 Magnetic stress tensor

In this section, the magnetic stress tensor is defined. The notion of magnetic stress tensor provides a mathematical framework for the calculation of the magnetic body-force density, surface-force density and resultant forces. In particular, the vacuum MST is presented.

### 2.1 MST

An elementary volume  $d\Omega$  is considered to be immersed in a magneto-static field. The volume is small enough such that the magnetic field and mechanical properties are nearly uniform over the volume. Considering an isothermal deformation of a bounding surface of  $d\Omega$ , a second-order stress tensor  $\mathbf{T}'$  is sought such that [7]:

$$\delta W = -\mathbf{n} \cdot \mathbf{T}' \cdot d\mathbf{x} \quad (1)$$

with  $\delta W$  the mechanical work of the bounding surface,  $\mathbf{n}$  the normal field to the bounding surface and  $d\mathbf{x}$  the infinitesimal displacement field. An illustration is provided in Figure 1.

Then, the stress tensor  $\mathbf{T}'$  can be decomposed as:

$$\mathbf{T}' = \mathbf{T}_{\text{mech}} + \mathbf{T}_{\text{m}}, \quad (2)$$

where  $\mathbf{T}_{\text{mech}}$  is the stress tensor associated with the deformation and  $\mathbf{T}_{\text{m}}$  is the magnetic stress tensor. It is supposed that  $\mathbf{T}_{\text{m}}$  depends only on magnetic properties – while  $\mathbf{T}_{\text{mech}}$  depends on mechanical properties – by considering a weak magneto-mechanical coupling.

According to refs. [7,8], it is possible to determine a symmetric  $\mathbf{T}_{\text{m}}$  by expressing  $\delta W$  with the electromechanical energy density of the system. Then, for incompressible linearly magnetizable media –  $\forall \mathbf{x} \in \Omega$ ,  $\mathbf{B}(\mathbf{x}) = \mu(\mathbf{x}, B)\mathbf{H}(\mathbf{x})$  – the magneto-static stress tensor reduces to the MST:

$$\mathbf{T}_{\text{m}} = \mathbf{H}\mathbf{B} - \frac{1}{2}|\mathbf{B}||\mathbf{H}|\mathbf{I}, \quad (3)$$

where  $\mathbf{I}$  is the identity tensor of order 2, using a tensor product between  $\mathbf{H}$  and  $\mathbf{B}$ . Another method to obtain (3)

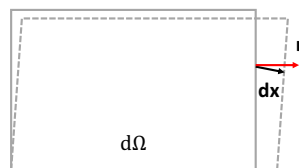


Figure 1: Illustration of mechanical work by deformation of an elementary volume.

is to look for a  $\mathbf{T}_m$  expression which is compatible with the Lorentz force [1,6]. The particular case of the vacuum MST is obtained for  $\mu = \mu_0$ . Finally, the MST can be expressed in a more practical way using a 2D cylindrical coordinate system [5]:

$$\mathbf{T}_m = \frac{1}{2\mu} \begin{pmatrix} B_r^2 - B_\theta^2 & 2B_r B_\theta \\ 2B_\theta B_r & B_\theta^2 - B_r^2 \end{pmatrix}. \quad (4)$$

## 2.2 Air-gap Maxwell tensor

The total magnetic force  $\mathbf{F}_m$  applied on a domain  $V$  can be obtained by integrating the divergence of  $\mathbf{T}_m$  into a volume  $\Omega$  containing  $V$ :

$$\mathbf{F}_m = \int_{\Omega} \nabla \cdot \mathbf{T}_m d\Omega. \quad (5)$$

Suppose  $\Omega$  is a compact subset of  $\mathbb{R}^3$  with a piece-wise smooth closed boundary  $\Gamma$ , and since  $\mathbf{T}_m$  is continuously differentiable on  $\Omega$  and defined on a neighborhood of  $\Omega$ , Gauss's theorem [38] can be applied:

$$\mathbf{F}_m = \oint_{\Gamma} \mathbf{T}_m \cdot \mathbf{n} d\Gamma, \quad (6)$$

where  $\mathbf{n}$  is the outward pointing unit normal field of the closed boundary  $\Gamma$ . If  $V$  is surrounded by non-magnetic material (for example, air or void), then  $\Gamma$  can be extended to this non-magnetic domain without changing the total magnetic force or torque acting on  $V$ .

In the case of electrical machine, the computed total force is the same for any continuous surface in the air gap, even one that wiggles and changes radius. If  $B_n$  and  $H_t$  are the magnetic fluxes locally normal (resp. magnetic field locally tangential) to  $\Gamma$ , then integrating the MST (3) along  $\Gamma$  in the air gap – as in Figure 2 – leads to:

$$\mathbf{F}_m = \int_{\Gamma} \left( -\frac{\mu_0}{2} H^2 \mathbf{n} + \mu_0 H_n \mathbf{H} \right) d\Gamma. \quad (7)$$

At this point, the term under the integral sign has the dimension of a surface force density denoted  $\mathbf{P}_{ag}$ . Developing  $\mathbf{P}_{ag}$  leads to:

$$\mathbf{P}_{ag} = \left( \frac{1}{2\mu_0} B_n^2 - \frac{\mu_0}{2} H_t^2 \right) \mathbf{n} + B_n H_t \mathbf{t}, \quad (8)$$

where  $\mathbf{t}$  is the unit tangential field associated with  $\mathbf{n}$ . Expression (8) is usually applied on a cylindrical surface  $\Gamma$  in the middle of the air gap [5,12–17,32]. An example is provided in Figure 2 with the blue dashed surface  $\Gamma$ . With

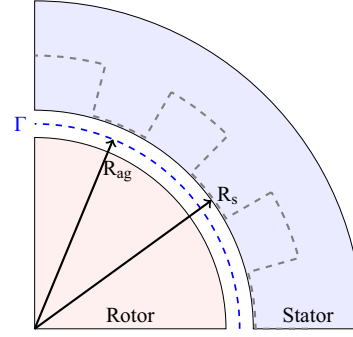


Figure 2: Illustration of the air-gap Maxwell tensor application.

cylindrical surfaces, the normal direction  $\mathbf{n}$  is opposite to the radial direction  $\mathbf{e}_r$  when considering the forces experienced by the external structure. Then, the surface force (8) can be decomposed as a sum of a radial and tangential contribution  $\forall \theta \in [0, 2\pi]$  and for all radius  $r$  inside the air-gap cylindrical band:

$$\mathbf{P}_{ag}(r, \theta) = P_r(r, \theta) \mathbf{e}_r + P_\theta(r, \theta) \mathbf{e}_\theta \quad (9)$$

such that the formula to compute AGSF becomes:

$$P_r(r, \theta) = -\left( \frac{1}{2\mu_0} B_r^2(r, \theta) - \frac{\mu_0}{2} H_\theta^2(r, \theta) \right), \quad (10)$$

$$P_\theta(r, \theta) = -B_r(r, \theta) H_\theta(r, \theta).$$

The advantage of using (10) is that global magnetic forces in the Cartesian referential – as well as electromagnetic torque – are theoretically independent of the selected closed surface  $\Gamma$ . On the other hand, the surface force density (10) varies depending on  $\Gamma$  [33,34].

### 2.2.1 Surface force density on tooth tip

The properties of  $\mathbf{T}_m$  allow us to compute the surface magnetic force density  $\mathbf{p}$  at the interface between domain 1 and domain 2 as illustrated in Figure 3. Indeed, a magnetic stress tensor  $\mathbf{T}_{m,1}$  associated with domain 1 generates a surface force density  $\mathbf{p}_1$  on  $\Gamma$ :

$$\mathbf{p}_1 = \mathbf{n}_{1,2} \cdot \mathbf{T}_1 = -\mathbf{n}_{2,1} \cdot \mathbf{T}_1, \quad (11)$$

where  $\mathbf{n}_{1,2}$  is the outward pointing unit normal vector. Another contribution  $\mathbf{p}_2$  is obtained when considering

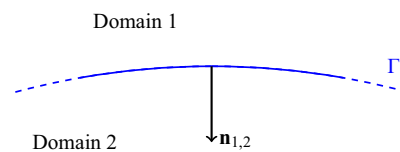


Figure 3: Surface force density calculation.

domain 2. The resultant surface force density  $\mathbf{P}_{\text{surf}}$  is obtained by applying (11) on both sides of  $\Gamma$ :

$$\mathbf{P}_{\text{surf}} = \mathbf{p}_1 + \mathbf{p}_2. \quad (12)$$

As a consequence, magnetic surface forces come from a permeability gap. In electrical machines, the magnetic surface forces of interest are mainly located on stator teeth tip at the interface between the air and ferromagnetic media:

$$\begin{aligned} \mathbf{p}_{\text{air}} &= \left\{ \frac{1}{2\mu_0} B_n^2 - \frac{\mu_0}{2} H_t^2 \right\} \mathbf{n}, \\ \mathbf{p}_{\text{iron}} &= - \left\{ \frac{1}{2\mu} B_n^2 - \frac{\mu}{2} H_t^2 \right\} \mathbf{n}. \end{aligned} \quad (13)$$

Then the surface force density applied to the ferromagnetic media becomes [8,39,40]:

$$\mathbf{P}_{\text{surf}} = \left\{ \frac{1}{2} \left( \frac{1}{\mu_0} - \frac{1}{\mu} \right) B_n^2 - \frac{\mu_0 - \mu}{2} H_t^2 \right\} \mathbf{n}. \quad (14)$$

Note that this expression should lead to the same results on both sides of the interface since  $B_n$  and  $H_t$  are theoretically continuous. If the assumption of high relative permeability in iron is used for the vibroacoustic design of electrical machines, such that  $\mu \rightarrow \infty$ , then there are two different possibilities:

- (1)  $\mu H_t^2 \rightarrow \infty$ ,
- (2)  $\mu H_t^2 \rightarrow 0$ .

If (1) is true, then it means that  $\frac{1}{\mu} B_t^2 \rightarrow \infty$ , implying  $B_t \rightarrow \infty$  which is not physical. By elimination, only (2)

can be true. As a consequence,  $\mathbf{p}_{\text{iron}} \rightarrow 0$ . Then (14) is usually approximated by:

$$\mathbf{P}_{\text{surf}} \approx \mathbf{p}_{\text{air}} \approx \left( \frac{1}{2\mu_0} B_n^2 - \frac{\mu_0}{2} H_t^2 \right) \mathbf{n}. \quad (15)$$

Then one gets for the angular position  $\theta$  corresponding to the tip of the stator teeth:

$$\mathbf{P}_{\text{surf}} = \mathbf{P}_{\text{ag}}(R_s, \theta). \quad (16)$$

As seen in ref. [32], magnetic forces are mainly concentrated on the tip of the stator teeth as surface forces in the case of low saturation (or high relative permeability). To reduce differences with the interface surface forces on the tooth tip (15), the AGSF (10) should be applied at the stator bore radius  $R_s$ . However, it is not possible when using analytical modeling. This is the main motivation for determining the AGSF transfer law (45).

Additionally, a transfer law could be useful even when considering electromagnetic FEA. Indeed, it is well-known that the electromagnetic field is ill-defined at the corner of a tooth because it comes off at an angle. Moreover, the weak formulation used in FEA does not allow us to impose both normal magnetic flux density  $B_n$  and tangential magnetic field  $H_t$  continuous at the same time. As a consequence, numerical errors increase near a discontinuity in magnetic permeability (e.g. on the tip of the teeth). An example of this issue is presented in Figures 4 and 5: it is based on the slotless case from ref. [34], in which the FEA is performed with FEMM [41]. The slotless geometry is chosen to prevent errors due to an ill-defined magnetic field in the corners. These errors affect both radial and tangential force evaluation. Vibration generated by radial forces is often

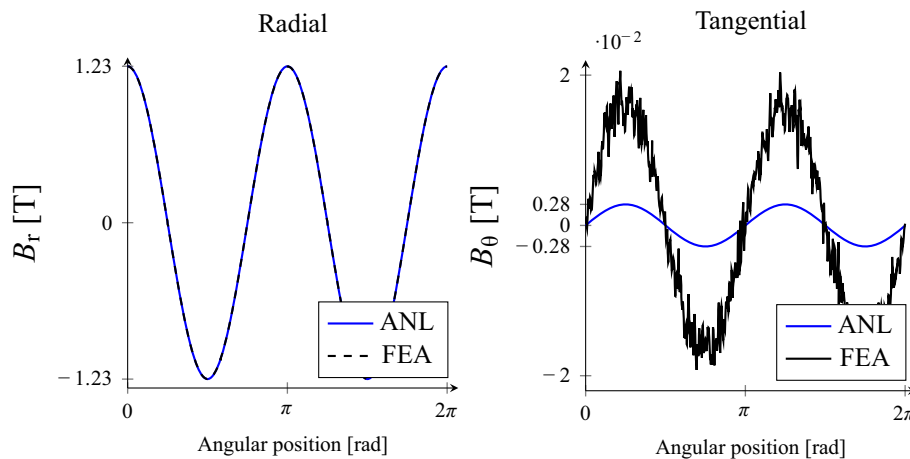


**Figure 4:** Comparison between analytical (ANL) and numerical (FEA) computations of the magnetic flux density components  $B_r$  and  $B_t$  at radius  $r = 0.9996R_s$  with a slotless machine for a wavenumber  $k = 2$ .

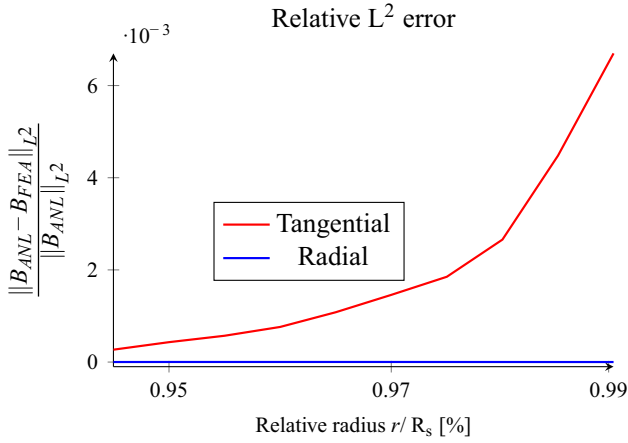


**Figure 5:** Comparison between analytical (ANL) and numerical (FEA) computations of the magnetic flux density components  $B_r$  and  $B_t$  depending on the radius with a slotless machine for a wave-number  $k = 2$ .

predominant; however, the tangential contribution should not be underestimated in the general case [29,42,43].

To reduce this numerical error, a thinner mesh can be used at the iron/air interface but this should increase the calculation time. Then calculating AGSF with the magnetic field in the middle of the air gap instead of the tooth tip distorted magnetic field can therefore reduce calculation cost. This is another motivation for determining the AGSF transfer law (45).

### 2.2.2 Application to vibroacoustic

Another reason for using the AGSF (10) based on MST is the compatibility with electromagnetic vibration synthesis (EVS) [28]. The principle of EVS is to excite a structural model – analytical cylindrical shell model [26,44], 3D mechanical FEA [14,29] – with some unit-magnitude rotating force waves. The targeted wavenumbers are generally between 0 and 8 for the vibroacoustic analysis of electrical machines. Finally, the EVS can be performed by multiplying each wavenumber of the AGSF complex Fourier transform with its corresponding FRF.

The magneto-mechanical coupling based on AGSF (10) combined with FRF is of great interest for the vibroacoustic study of electrical machines because it allows a troubleshooting of the vibroacoustic behavior from several electromagnetic sources based on the air-gap spectrum [44–46]. In particular, the tangential force response is also under investigation because it can be a significant contributor to the magnetic noise [14,29,30,42,43,47].

For all these motivations, the next sections propose to demonstrate and apply a new transfer law in order to understand the surface force behavior in the air gap.

## 3 Demonstration of transfer coefficients

The goal of this section is to analytically demonstrate the transfer law (45) and the associated transfer coefficients (46). It is supposed that the AGSF (10) is known on a circular contour in the air gap such as the blue contour  $\Gamma$  in Figure 2. To demonstrate the transfer law, the air-gap magnetic field is analytically solved with the approximation of quasi-stationary regimes and without any hypothesis on the electrical machine topology. Then the complex Fourier transform of the AGSF is computed at both air-gap radius  $R_{ag}$  and  $R_s$ . Finally, the different expressions are compared to get the transfer law (45). The temporal dimension is omitted because formulae remain valid at any time step. Mathematical tools and formulations are borrowed from the publications [23,48–50].

### 3.1 Magnetic field in the air gap

The definition, domain required for the problem is reduced to the cylindrical air-gap band. At first, a single magnetic flux density wave of order  $k$  is considered as the boundary condition in the air gap at the radius  $r = R_{ag}$ :

$$\begin{aligned} B_r(R_{ag}, \theta) &= B_{r,k} \cos(k\theta + \phi_{r,k}), \\ B_\theta(R_{ag}, \theta) &= B_{\theta,k} \cos(k\theta + \phi_{\theta,k}). \end{aligned} \quad (17)$$

It is equivalent to say that an ideal excitation is considered. It can be produced by any kind of component (electrical conductor and permanent magnets) but this study does not make any distinction. Note that the radius  $R_{ag}$  is arbitrarily chosen in the domain of definition.

Under these conditions, the fundamental equation for the electromagnetic field is Poisson's equation [38] for the 2D magnetic vector potential component  $A_z$  in polar coordinates  $\forall \theta \in [0, 2\pi]$ ,  $\forall r \in [R_{ag}, R_s]$ :

$$\frac{1}{r} \frac{\partial}{\partial r} \left( \frac{1}{r} \frac{\partial A_z}{\partial r} \right) + \frac{\partial^2 A_z}{\partial \theta^2} = 0. \quad (18)$$

A solution exists and it is unique for the previous system [51]. Then a method consists to state a function  $A_z$  and to

check if it fulfills the boundary conditions. A solution similar to ref. [23] is searched for the upper cylindrical air-gap band  $\forall \theta \in [0, 2\pi]$  and  $\forall r \in [R_{ag}, R_s]$ :

$$A(r, \theta) = \frac{\gamma_k E_k(r, R_s) + \alpha_k E_k(R_{ag}, r)}{E_k(R_{ag}, R_s)} \sin(k\theta + \phi_{r,k}) + \frac{\zeta_k E_k(r, R_s) + \chi_k E_k(R_{ag}, r)}{E_k(R_{ag}, R_s)} \cos(k\theta + \phi_{\theta,k}), \quad (19)$$

where the unknowns  $\gamma_k$ ,  $\alpha_k$ ,  $\zeta_k$  and  $\chi_k$  depend on the geometry, the wavenumber and the boundary conditions. Next step is to link the magnetic flux density with the magnetic potential:

$$B_r(r, \theta) = \frac{1}{r} \frac{\partial A}{\partial \theta}(r, \theta), \quad (20)$$

$$B_\theta(r, \theta) = -\frac{\partial A}{\partial r}(r, \theta).$$

Then, the boundary condition (17) allows us to determine the previous unknowns:

$$\begin{aligned} \gamma_k &= \frac{R_{ag}}{k} B_{r,k}, \\ \alpha_k &= \frac{R_{ag}}{k} B_{r,k} \frac{F_k(R_{ag}, R_s)}{2}, \\ \zeta_k &= 0, \\ \chi_k &= \frac{R_{ag}}{k} B_{\theta,k} \frac{E_k(R_{ag}, R_s)}{2}. \end{aligned} \quad (21)$$

Thus, the magnetic potential inside the air-gap band is entirely determined. The corresponding magnetic flux density is deduced from the knowledge of (19) and (21):

$$\begin{aligned} B_r(R_s, \theta) &= \frac{R_{ag}}{R_s} \left( B_{r,k} \frac{F_k(R_{ag}, R_s)}{2} \cos(k\theta + \phi_{r,k}) - B_{\theta,k} \frac{E_k(R_{ag}, R_s)}{2} \sin(k\theta + \phi_{\theta,k}) \right) \\ B_\theta(R_s, \theta) &= \frac{R_{ag}}{R_s} \left( B_{r,k} \frac{E_k(R_{ag}, R_s)}{2} \sin(k\theta + \phi_{r,k}) + B_{\theta,k} \frac{F_k(R_{ag}, R_s)}{2} \cos(k\theta + \phi_{\theta,k}) \right). \end{aligned} \quad (22)$$

This result is generalizable to a multi-wavenumber magnetic problem, thanks to the linear property of Poisson equation [38,51]: a linear combination of solutions of the form (22) for different values of  $n$  is still a solution of (18). Using the following complex notation:

$$\begin{aligned} \underline{B}_{r,k} &= B_{r,k} e^{j\phi_{r,k}} \\ \underline{B}_{\theta,k} &= B_{\theta,k} e^{j\phi_{\theta,k}} \end{aligned} \quad (23)$$

the air-gap magnetic flux density can be decomposed as complex Fourier series:

$$\begin{aligned} B_r(R_{ag}, \theta) &= \sum_{k=-\infty}^{k=+\infty} \underline{B}_{r,k} e^{jk\theta}, \\ B_\theta(R_{ag}, \theta) &= \sum_{k=-\infty}^{k=+\infty} \underline{B}_{\theta,k} e^{jk\theta}. \end{aligned} \quad (24)$$

Note that the time variation is included in the phase terms  $\phi_{\theta,k}$  and  $\phi_{r,k}$ .

In the rest of the article, the following notation is used:

$$\begin{aligned} F_k &= F_k(R_{ag}, R_s), \\ E_k &= E_k(R_{ag}, R_s). \end{aligned} \quad (25)$$

Then the magnetic flux density on the stator bore radius  $R_s$  can be expressed as:

$$\begin{aligned} B_r(R_s, \theta) &= \frac{R_{ag}}{R_s} \sum_{k=-\infty}^{k=+\infty} \frac{F_k \underline{B}_{r,k} + jE_k \underline{B}_{\theta,k}}{2} e^{jk\theta}, \\ B_\theta(R_s, \theta) &= \frac{R_{ag}}{R_s} \sum_{k=-\infty}^{k=+\infty} \frac{F_k \underline{B}_{\theta,k} - jE_k \underline{B}_{r,k}}{2} e^{jk\theta}. \end{aligned} \quad (26)$$

The theoretic magnetic flux density on the stator bore radius  $R_s$  is obtained, thanks to (26) which is based on the air-gap boundary condition (24). The expression (26) is different from what can be found in the literature because it is based on the magnetic flux density instead of magnetic potential [23,52]. Using the magnetic flux density is necessary in this study since the AGSF expression (8) is based on the flux density.

Thus, (26) gives the theoretical spatial transfer of the magnetic flux density  $\mathbf{B}$  from the air-gap radius  $R_{ag}$  to the stator bore radius  $R_s$ . The goal of the next sections is to deduce from (26) the theoretical spatial transfer law for the AGSF radial component.

### 3.2 Radial magnetic surface forces

The magnetic radial surface force density experienced by the outer structure (stator or rotor) is computed according to the AGSF equation (10) on a contour of radius  $R_s$  corresponding to the stator teeth tip radius as in Figure 2:

$$P_r(R_s, \theta) = -\frac{B_r(R_s, \theta)^2 - B_\theta(R_s, \theta)^2}{2\mu_0}. \quad (27)$$

Note the sign of the equation taking into account the scalar product ( $\mathbf{n} \cdot \mathbf{e}_r = -1$ ) between the external normal to the surface  $\Gamma$  and the radial direction. The complex

Fourier transform of  $P_r$  is performed using the convolution product:

$$\hat{P}_r(R_s, n) = -\frac{[\hat{B}_r \otimes \hat{B}_r](R_s, n) - [\hat{B}_\theta \otimes \hat{B}_\theta](R_s, n)}{2\mu_0}, \quad (28)$$

where  $\hat{B}_r$  and  $\hat{B}_\theta$  are the complex Fourier transform of  $B_r$  and  $B_\theta$ . Using properties of convolution product,  $\hat{P}_r$  is written as:

$$\hat{P}_r(R_s, n) = -\left(\frac{R_{ag}}{R_s}\right)^2 \frac{1}{8\mu_0} \sum_{k=-\infty}^{k=+\infty} P_{r,k,n} e^{jn\theta}, \quad (29)$$

where  $P_{r,k,n}$  is expressed using (26):

$$\begin{aligned} P_{r,k,n} &= (F_k F_{n-k} + E_k E_{n-k}) \underline{B}_{r,k} \underline{B}_{r,n-k} \\ &\quad - (F_k F_{n-k} + E_k E_{n-k}) \underline{B}_{\theta,k} \underline{B}_{\theta,n-k} \\ &\quad + j(F_k E_{n-k} + E_k F_{n-k}) \underline{B}_{r,k} \underline{B}_{\theta,n-k} \\ &\quad + j(F_k E_{n-k} + E_k F_{n-k}) \underline{B}_{r,n-k} \underline{B}_{\theta,k}. \end{aligned} \quad (30)$$

At this point, the spatial variation of each AGSF wave-number is complex because it depends on the recombination of several magnetic flux density waves. Nevertheless, using polynomial properties of  $F_k$  and  $E_k$ , it can be shown:

$$\begin{cases} F_k F_{n-k} + E_k E_{n-k} = 2F_n \\ F_k E_{n-k} + E_k F_{n-k} = 2E_n \end{cases} \quad (31)$$

such that  $P_{r,k,n}$  can be factorized:

$$\begin{aligned} P_{r,k,n} &= 2F_n (\underline{B}_{r,k} \underline{B}_{r,n-k} - \underline{B}_{\theta,k} \underline{B}_{\theta,n-k}) \\ &\quad + j2E_n (\underline{B}_{r,k} \underline{B}_{\theta,n-k} + \underline{B}_{r,n-k} \underline{B}_{\theta,k}). \end{aligned} \quad (32)$$

The convolution product is used to factorize the sum:

$$\begin{aligned} \sum_{k=-\infty}^{k=+\infty} P_{r,k,n} &= 2F_n [\hat{B}_r \otimes \hat{B}_r](R_{ag}, n) + 2F_n [\hat{B}_\theta \otimes \hat{B}_\theta] \\ &\quad \times (R_{ag}, n) + j4E_n [\hat{B}_r \otimes \hat{B}_\theta](R_{ag}, n). \end{aligned} \quad (33)$$

Replacing this intermediate result in (29) leads to:

$$\begin{aligned} \hat{P}_r(R_s, n) &= -\frac{1}{2} \left(\frac{R_{ag}}{R_s}\right)^2 F_n \frac{1}{2\mu_0} ([\hat{B}_r \otimes \hat{B}_r](R_{ag}, n) \\ &\quad - [\hat{B}_\theta \otimes \hat{B}_\theta](R_{ag}, n)) \\ &\quad - j \frac{1}{2} \left(\frac{R_{ag}}{R_s}\right)^2 E_n \frac{1}{\mu_0} [\hat{B}_r \otimes \hat{B}_\theta](R_{ag}, n). \end{aligned} \quad (34)$$

Then the air-gap MST terms (10) are identified:

$$\hat{P}_r(R_s, n) = \left(\frac{R_{ag}}{R_s}\right)^2 \frac{F_n \hat{P}_r(R_{ag}, n) + jE_n \hat{P}_\theta(R_{ag}, n)}{2}. \quad (35)$$

Introducing the self-transfer coefficient  $S_n$ :

$$S_n = \left(\frac{R_{ag}}{R_s}\right)^2 \frac{F_n}{2} = \frac{1}{2} \left(\frac{R_{ag}}{R_s}\right)^{n+2} + \frac{1}{2} \left(\frac{R_{ag}}{R_s}\right)^{-n+2} \quad (36)$$

and the cross-transfer coefficient  $C_n$ :

$$C_n = \left(\frac{R_{ag}}{R_s}\right)^2 \frac{E_n}{2} = \frac{1}{2} \left(\frac{R_{ag}}{R_s}\right)^{n+2} - \frac{1}{2} \left(\frac{R_{ag}}{R_s}\right)^{-n+2}, \quad (37)$$

formula (35) can be rewritten in the form:

$$\hat{P}_r(R_s, n) = S_n \hat{P}_r(R_{ag}, n) + jC_n \hat{P}_\theta(R_{ag}, n), \quad (38)$$

which demonstrates the radial part of (45). Note that the limit case  $R_{ag} = R_s$  leads to  $S_n = 1$  and  $C_n = 0$  such that  $\hat{P}_r(R_s, n) = \hat{P}_r(R_{ag} = R_s, n)$ . Thus, the formula stays valid.

### 3.3 Tangential magnetic surface forces

The magnetic tangential surface force experienced by the outer structure is computed according to the MST formula:

$$P_\theta(R_s, \theta) = -\frac{B_r(R_s, \theta) B_\theta(R_s, \theta)}{\mu_0}. \quad (39)$$

The methodology is very similar to the radial case. The complex Fourier transform of  $P_\theta$  is performed using the convolution product:

$$\hat{P}_\theta(R_s, n) = -\frac{[\hat{B}_r \otimes \hat{B}_\theta](R_s, n)}{\mu_0}, \quad (40)$$

which can be rewritten as:

$$\hat{P}_\theta(R_s, n) = -\frac{1}{4\mu_0} \left(\frac{R_{ag}}{R_s}\right)^2 \sum_{k=-\infty}^{k=+\infty} P_{\theta,k,n} e^{jn\theta} \quad (41)$$

with  $P_{\theta,k,n}$  expressed using (26)

$$\begin{aligned} P_{\theta,k,n} &= 2F_n \underline{B}_{r,k} \underline{B}_{\theta,n-k} - jE_n (\underline{B}_{r,k} \underline{B}_{r,n-k} \\ &\quad - \underline{B}_{\theta,k} \underline{B}_{\theta,n-k}). \end{aligned} \quad (42)$$

Replacing this intermediate result in (41) leads to:

$$\begin{aligned} \hat{P}_\theta(R_s, n) &= -\left(\frac{R_{ag}}{R_s}\right)^2 \left( E_n \frac{1}{2\mu_0} [\hat{B}_r \otimes \hat{B}_\theta](R_{ag}, n) \right. \\ &\quad \left. + jF_n \frac{1}{4\mu_0} ([\hat{B}_r \otimes \hat{B}_r](R_{ag}, n) \right. \\ &\quad \left. - [\hat{B}_\theta \otimes \hat{B}_\theta](R_{ag}, n)) \right). \end{aligned} \quad (43)$$

Finally, identifying air-gap MST terms and using coefficients (36) and (37) lead to:

$$\hat{P}_\theta(R_s, n) = S_n \hat{P}_\theta(R_{ag}, n) - jC_n \hat{P}_r(R_{ag}, n), \quad (44)$$

which demonstrates the tangential part of (45). Note that the limit case  $R_{ag} = R_s$  leads to  $S_n = 1$  and  $C_n = 0$  such that  $\hat{P}_\theta(R_s, n) = \hat{P}_\theta(R_{ag} = R_s, n)$ . Thus, the formula stays valid.

### 3.4 Discussion

This section aims to analyze the previous results in order to determine how it could affect the computed AGSF. In order to obtain equations (44) and (38), an electrical machine with a cylindrical air-gap band was considered. A particular example with polar teeth is given in Figure 2 but any machine topology could be considered. Equations (44) and (38) compose the new transfer law:

$$\begin{aligned}\hat{P}_r(R_s, n) &= S_n \hat{P}_r(R_{ag}, n) + jC_n \hat{P}_\theta(R_{ag}, n), \\ \hat{P}_\theta(R_s, n) &= S_n \hat{P}_\theta(R_{ag}, n) - jC_n \hat{P}_r(R_{ag}, n),\end{aligned}\quad (45)$$

where  $S_n$  is called the self-transfer coefficient and  $C_n$  the cross-transfer coefficient:

$$\begin{aligned}S_n &= \frac{1}{2} \left\{ \left( \frac{R_{ag}}{R_s} \right)^{n+2} + \left( \frac{R_{ag}}{R_s} \right)^{-n+2} \right\}, \\ C_n &= \frac{1}{2} \left\{ \left( \frac{R_{ag}}{R_s} \right)^{n+2} - \left( \frac{R_{ag}}{R_s} \right)^{-n+2} \right\}.\end{aligned}\quad (46)$$

These coefficients  $S_n$  and  $C_n$  only depend on the considered magnetic surface force wavenumber  $n$  and the adimensional radius ratio  $r = \frac{R_{ag}}{R_s}$ . Thus, the spatial variation of AGSF does not depend on a particular combination of magnetic flux density  $k$ th wavenumbers but only on the considered AGSF wavenumber  $n$ . It also confirms that radial and tangential magnetic surface forces are strongly correlated.

This result is a generalization of the simplified coefficients which were found in ref. [34] but the new transfer coefficients include tangential surface force density and are valid for any kind of topology. The results of ref. [34] can be found back assuming  $P_\theta(R_s, \theta) = 0 \quad \forall \theta \in [0, 2\pi]$ .

Figures 6–8 illustrate the variation of the transfer coefficients (36) and (37) with the wavenumber  $n$  and

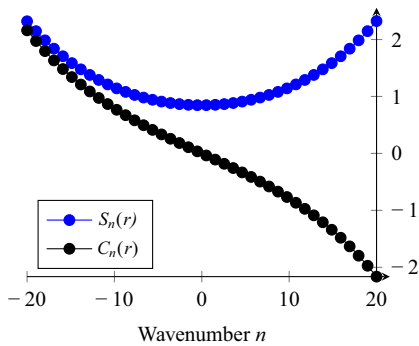


**Figure 6:** Transfer coefficients at a fixed relative radius  $r = \frac{R_{ag}}{R_s} = 0.96$ .

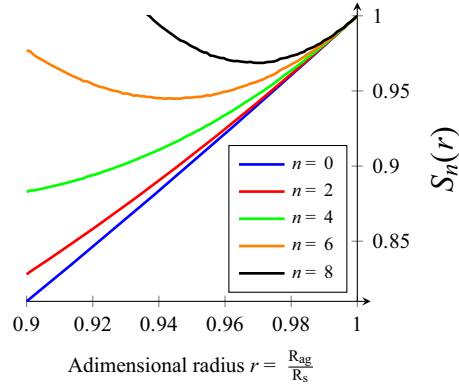


**Figure 7:** Self-transfer coefficient  $S_n(r)$  as a function of adimensional radius  $r$ .

the adimensional radius  $r$ . In particular, Figure 6 highlights that:

$$\begin{aligned}\lim_{|n| \rightarrow \infty} |S_n| &= \infty, \\ \lim_{|n| \rightarrow \infty} |C_n| &= \infty.\end{aligned}\quad (47)$$

Theoretically, the number of wavenumbers in the air gap is not infinite such that:

$$\begin{aligned}\lim_{|n| \rightarrow \infty} |S_n \hat{P}_r(R_{ag}, n) + jC_n \hat{P}_\theta(R_{ag}, n)| &= 0, \\ \lim_{|n| \rightarrow \infty} |S_n \hat{P}_\theta(R_{ag}, n) - jC_n \hat{P}_r(R_{ag}, n)| &= 0.\end{aligned}\quad (48)$$

Nevertheless, the computation of numerical FFT does not provide an exact zero at every non-physical frequency. Then it is recommended to take precautions to avoid numerical noise amplification at high wavenumbers.

As illustrated in Figure 6, the transfer coefficients have the following symmetry properties:

$$\begin{aligned}S_{-n} &= S_n, \\ C_{-n} &= -C_n.\end{aligned}\quad (49)$$

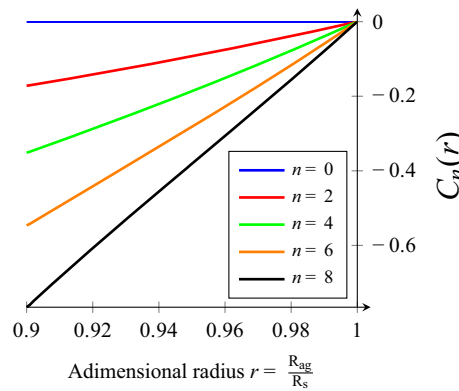


**Figure 8:** Cross-transfer coefficient  $C_n(r)$  as a function of adimensional radius  $r$ .

The resultant electromagnetic torque is independent of the radius, as expected from the MST:

$$\begin{aligned} M_z(R_s) &= \int_0^{2\pi} P_\theta(R_s, \theta) R_s^2 d\theta \\ &= 2\pi \hat{P}_\theta(R_s, 0) R_s^2 \\ &= 2\pi \left( \frac{R_{ag}}{R_s} \right)^2 \hat{P}_\theta(R_{ag}, 0) R_s^2 \\ &= M_z(R_{ag}). \end{aligned} \quad (50)$$

The authors recall that this result is valid for any closed path in the air gap according to Stoke's theorem. However, the total radial  $F_r$  or total tangential  $F_t$  forces computed with AGSF depend on the radius:

$$\begin{aligned} F_r(R_s) &= \int_0^{2\pi} P_r(R_s, \theta) R_s d\theta \\ &= 2\pi \hat{P}_r(R_s, 0) R_s \\ &= 2\pi \left( \frac{R_{ag}}{R_s} \right)^2 \hat{P}_r(R_{ag}, 0) R_s \\ &= \frac{R_{ag}}{R_s} F_r(R_{ag}) \end{aligned} \quad (51)$$

and similarly,

$$F_\theta(R_s) = \frac{R_{ag}}{R_s} F_\theta(R_{ag}). \quad (52)$$

Indeed, Stoke's theorem is theoretically valid for global forces  $F_x$  and  $F_y$  in the fixed Cartesian coordinate frame:

$$\begin{aligned} F_x(R_s) &= \int_0^{2\pi} (P_r(R_s, \theta) \cos(\theta) - P_\theta(R_s, \theta) \sin(\theta)) R_s d\theta \\ &= F_x(R_{ag}), \\ F_y(R_s) &= \int_0^{2\pi} (P_r(R_s, \theta) \sin(\theta) + P_\theta(R_s, \theta) \cos(\theta)) R_s d\theta \\ &= F_y(R_{ag}). \end{aligned} \quad (53)$$

Nevertheless, in most of the electrical machines  $\frac{R_{ag}}{R_s} \approx 1$  such that the approximations  $F_r(R_s) \approx F_r(R_{ag})$  and  $F_\theta(R_s) \approx F_\theta(R_{ag})$  can be used accurately for vibroacoustic assessment [14,32]. Indeed, the air-gap cylindrical band thickness  $g$  is generally very small compared to the stator bore radius  $R_s$  such that the following approximations can be made:

$$\begin{aligned} S_n &\approx 1, \\ C_n &\approx -n \frac{g}{R_s}. \end{aligned} \quad (54)$$

These approximations allow us to have an a priori estimation of the transfer error on the computed AGSF. To

illustrate the relevance of this estimation, an electrical machine with a single wavenumber excitation  $n$  is considered:

$$\begin{aligned} \hat{P}_r(R_s, n) &= jM \hat{P}_\theta(R_{ag}, n), \\ \frac{g}{R_s} &= \frac{1}{Q}, \end{aligned} \quad (55)$$

where  $M \gg 1$  and  $Q \gg 1$  are adimensional coefficients. Introducing (54) in (38) and (44) leads to:

$$\begin{aligned} |\hat{P}_r(R_s, n)| &\approx |\hat{P}_r(R_{ag}, n)| \\ |\hat{P}_\theta(R_s, n)| &\approx \left( 1 + n \frac{M}{Q} \right) |\hat{P}_\theta(R_{ag}, n)|. \end{aligned} \quad (56)$$

It means that depending on the  $\frac{M}{Q}$  ratio, the transfer coefficients could have a great influence on the tangential magnetic force. A numerical application with the topology studied in ref. [32] shows that  $\frac{M}{Q} \approx \frac{1}{10}$  such that there could be a 40% error on the fourth wavenumber.

In summary, the transfer law (45) was demonstrated. Then the transfer coefficients were analyzed. In particular, Taylor expansions were performed to show that the transfer law effect on AGSF is not necessarily negligible. Consequently, a more detailed numerical study is carried out in the following section.

## 4 Application to electrical machines

In order to check if the transfer law (45) can have a non-negligible impact on the vibroacoustic behavior of an electrical machine, this section presents two numerical applications:

- An induction machine with a constructive effect of coefficients (45).
- A synchronous machine with a destructive effect of coefficients (45).

As the aim of this section is to numerically validate the new transfer law, a reference is required. As discussed in ref. [32], the nodal force based on virtual work principle (VWP) [9] is commonly assumed to be the most accurate method for magnetic force computation because it has shown to be robust with respect to formulation: according to ref. [53] the VWP requires only one field component either  $\mathbf{H}$  (in scalar potential  $\phi$ -formulation) or  $\mathbf{B}$  (in vector potential A-formulation) to compute magnetic forces.

However, the VWP output physical unit is in (N/m) for a 2D FEA simulation, while the AGSF gives (N/m<sup>2</sup>). The

next section proposes a methodology to build equivalent surface force density from VWP result.

#### 4.1 VWP equivalent surface force

According to ref. [54], the nodal force computed with the VWP concentrates the effects of the actual force density in the direct vicinity of the node. As a consequence, a nodal force is meaningful only on its original mesh. Then VWP nodal forces must be converted in order to be compared with the MST which is a surface force density defined on a contour in the air gap.

The proposed method consists in summing all the nodal forces from VWP included in an angular opening  $d\theta$  to get the corresponding total force  $F_{d\theta}$  as shown in Figure 9. Then the obtained force is divided by the equivalent tooth tip surface:

$$P_{d\theta} = \frac{F_{d\theta}}{R_s d\theta}. \quad (57)$$

The computed magnetic surface force density depends on the radius of the targeted surface, but this is not a problem if the barycenter of the forces is very close to  $R_s$  [32]. The idea is to apply this process according to the discretization of the air-gap MST such that a surface force density  $P_{vwp}(\theta) \forall \theta \in [0, 2\pi]$  is obtained on the stator bore radius  $R_s$ .

#### 4.2 Validation with SCIM

In this section, different methods for computing the magnetic radial and tangential surface force density are compared. The simulation was performed with FEA using MANATEE-FEMM coupling [41,55]. The authors remind that FEMM simulations are performed using a potential vector A-formulation.

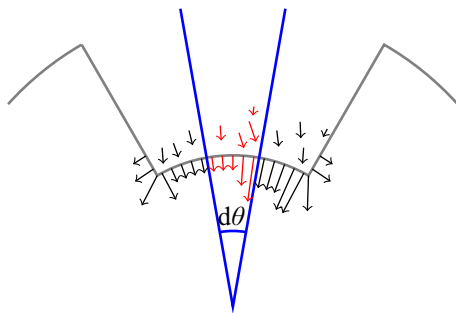


**Figure 9:** Summing all nodal forces (red arrows) on an angular opening  $d\theta$  to get an equivalent surface force density at stator bore radius.

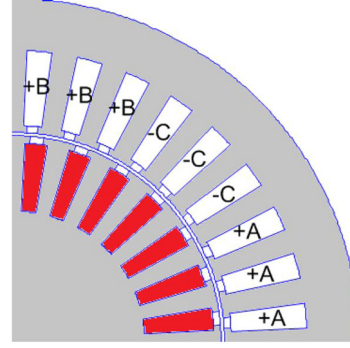


**Figure 10:** Analyzed cage rotor induction machine with single layer winding and stator/rotor semiclosed slots (one pole) [24].

A topology where the air-gap MST is commonly used to compute magnetic surface forces is the SCIM characterized by a thin cylindrical air-gap band ( $\frac{g}{R_s} \approx 1\%$ ). In particular, the studied SCIM topology is presented in Figure 10.

The magnetic AGSF is computed according to different methods named as follows:

- VWP-S: the reference is the VWP equivalent surface force density as presented in Section 4.1;
- AGSF-TR: the new method to transfer AGSF (8) from  $R_{ag}$  to  $R_s$  using transfer coefficients (45);
- AGSF- $R_{ag}$ : AGSF (8) applied on a circular contour at radius  $R_{ag}$  in the middle of the air-gap cylindrical band;
- AGSF- $R_s$ : AGSF (8) applied on a circular contour at a radius  $r = 0.9997R_s$  i.e. cutting through the first layer of air-gap element at the tooth tip.

The results are presented in Figure 11 for the radial direction and in Figure 12 for the tangential direction. In particular, Figure 13 focuses on the force lower wavenumbers of interest for vibroacoustic analysis.

A global observation of the results indicates that the AGSF- $R_{ag}$  is giving more accurate radial surface force than AGSF- $R_s$  for low wavenumbers. However, the AGSF- $R_s$  is more accurate than AGSF- $R_{ag}$  for tangential surface force. In both directions, the AGSF-TR is accurate. In order to quantify these observations, a norm is defined to quantify the deviation from the VWP-S method:

$$\|\hat{P} - \hat{P}_{vwp}\|_N = \sum_{k=-N}^{k=+N} |\hat{P}(k) - \hat{P}_{vwp}(k)|. \quad (58)$$

The first eight wavenumbers have the main contribution to the total vibration. Then, two applications of (58) can be defined:

- $\|\cdot\|_8$  with the first eight wavenumbers.
- $\|\cdot\|_{254}$  with all available wavenumbers.

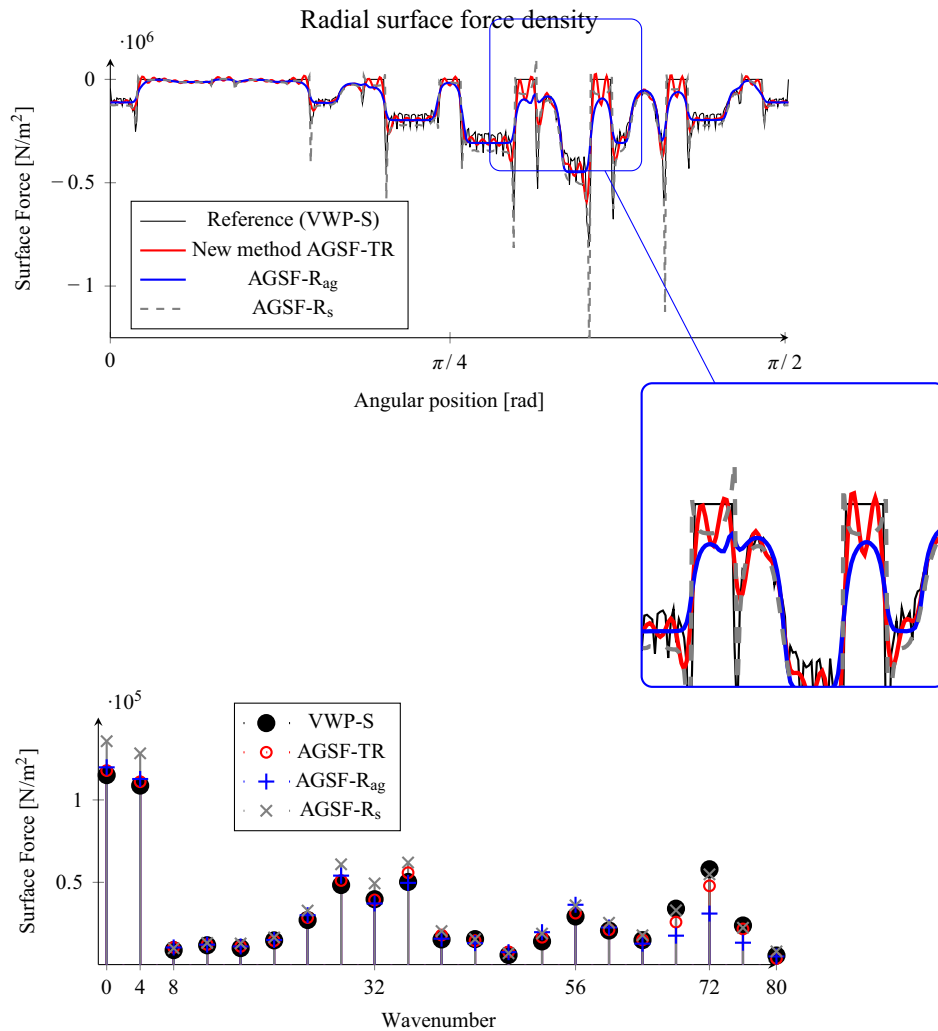


**Figure 11:** Comparison of several methods for radial surface force density using air-gap MST and VWP for SCIM topology.

It leads to the numerical values of Table 1 for radial AGSF and Table 2 for tangential AGSF. In all cases, the most accurate method is the AGSF-TR based on the new transfer law (45).

The benefits of the transfer coefficients used with AGSF-TR are particularly well shown in Figure 13, where the fourth wavenumber of the tangential AGSF is initially wrongly estimated by the AGSF- $R_{ag}$  method. When the AGSF-TR method is used based on (45), the fourth wavenumber of the radial surface force has a constructive interference with the fourth wavenumber of the tangential surface force in the air gap, thanks to the cross-transfer coefficient.

As the air gap is thin, previous results show that the effect of transfer law (45) remains weak on the radial AGSF. However, the effect of the transfer law is not

negligible on the tangential AGSF and leads to a clear improvement.

### 4.3 Application with SPMSM

This section proposes to compare the result of the different methods with an SPMSM topology. The topology used for this application is similar to that in ref. [31], except that the pole pair number was fixed to be eight and the simulation was performed at no-load as shown in Figure 15. In these conditions, Figures 14 and 16 give an image of the magnetic AGSF. The impact of the cross-transfer coefficients is noticeable: the eighth wavenumber of the radial AGSF in Figure 14 has a destructive interference with the eighth wavenumber of the tangential surface

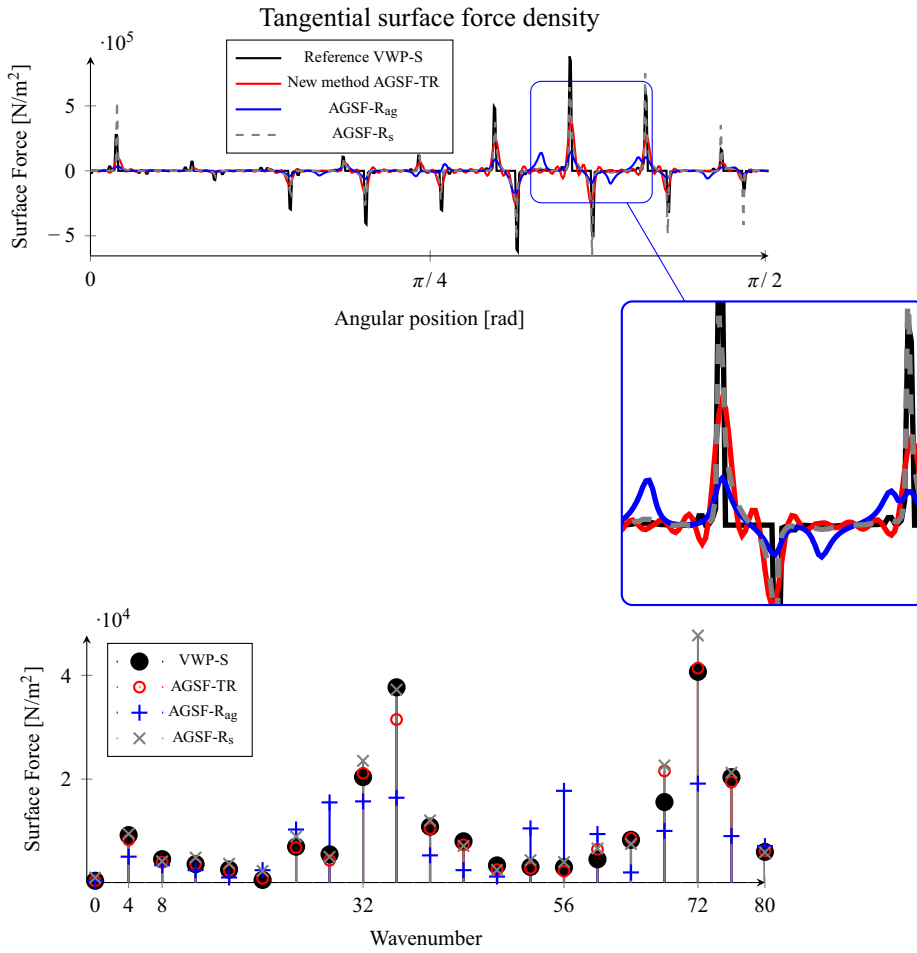


Figure 12: Comparison of several methods for tangential surface force density using air-gap MST and VWP for SCIM topology.

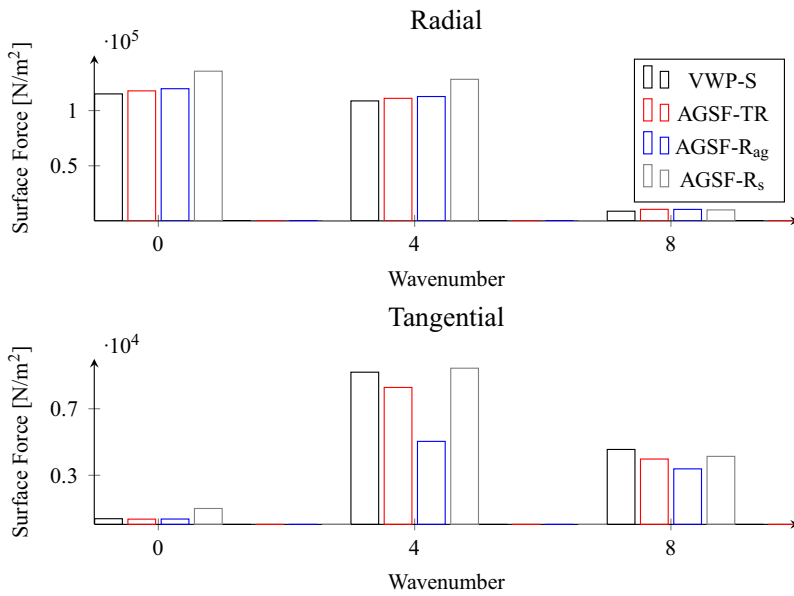


Figure 13: Comparison of several methods for surface force density for low wavenumbers with SCIM topology.

**Table 1:** Deviation of the magnetic surface force ( $\text{N}/\text{m}^2$ ) with respect to the VWP-S in the radial direction

Method	$\ \cdot\ _8$	$\ \cdot\ _{254}$
AGSF-TR	$1.3 \times 10^4$	$4.7 \times 10^5$
AGSF- $R_{\text{ag}}$	$1.8 \times 10^4$	$8.8 \times 10^5$
AGSF- $R_s$	$6.3 \times 10^4$	$6.3 \times 10^5$

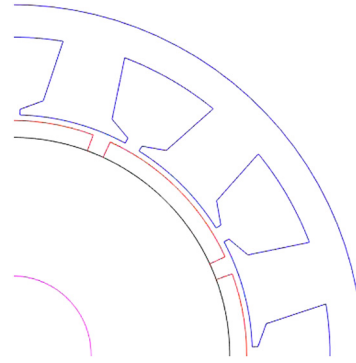
**Table 2:** Deviation of the magnetic air-gap surface force ( $\text{N}/\text{m}^2$ ) with respect to the VWP-S in the tangential direction

Method	$\ \cdot\ _8$	$\ \cdot\ _{254}$
AGSF-TR	$3.3 \times 10^3$	$4.1 \times 10^5$
AGSF- $R_{\text{ag}}$	$1.1 \times 10^4$	$8.9 \times 10^5$
AGSF- $R_s$	$4.0 \times 10^3$	$5.0 \times 10^5$

force in the air gap. Thus, the contribution of the cross-transfer coefficient (46) is again not negligible.

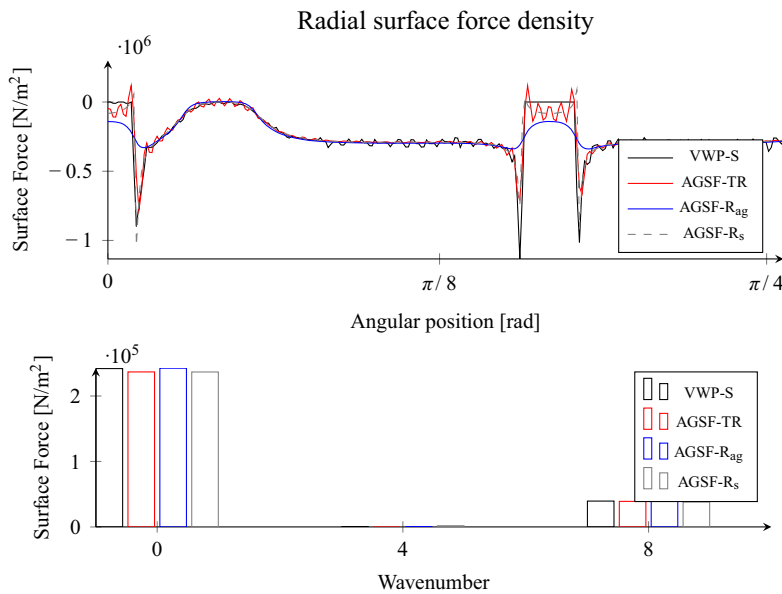
## 5 Conclusion

The purpose of this study was to improve the accuracy of the AGSFs computed with MST, thanks to the analytical study of the air-gap magnetic field. The analytical solution of the electromagnetic field in the air-gap cylindrical band

**Figure 15:** Analyzed surface permanent magnet synchronous machine with 12 slots and 8 poles.

was used to demonstrate the existence of a new transfer law depending on the radius and the wavenumbers. As expected, the transfer law has no impact on the torque calculation or the calculation of forces in the Cartesian coordinate frame. An induction machine and a synchronous machine were numerically simulated to evaluate the accuracy brought by the new transfer law on the magnetic AGSF: it has a strong influence on the tangential surface force whereas little influence on the radial surface force for the studied topologies.

The novelty of the proposed transfer law is to express AGSF wavenumbers as a function of the radius. Thus, the proposed transfer law provides a better understanding of the AGSFs. Indeed, the study analytically establishes that the AGSF wavenumbers are the same throughout the air

**Figure 14:** Comparison of several methods for radial surface force density using AGSF and VWP for SPMSM topology.

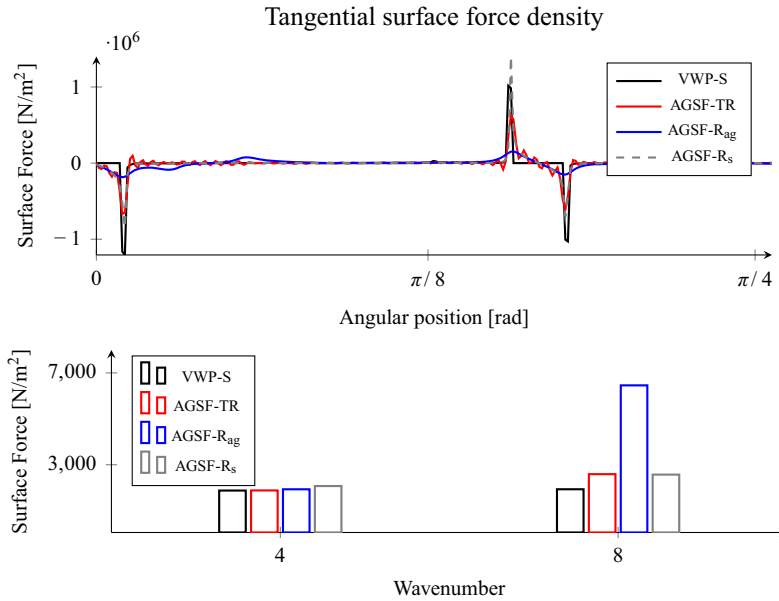


**Figure 16:** Comparison of several methods for tangential surface force density using AGSF and VWP for SPMSM topology.

gap, but that the amplitude of each AGSF harmonic depends on the radius of application according to the proposed transfer law. Therefore, the transfer law is interesting for FEA: the compromise between accuracy and numerical noise for AGSF – by choosing a radius of computation in the air gap – is not an issue anymore.

The transfer law opens the possibility to compute surface force based on MST with large equivalent air-gap machines such as salient pole alternators or switched reluctance machines. As a consequence, it allows us to improve the accuracy of vibroacoustic prediction and troubleshoot with analytical magnetic models.

Future research work will concern the compatibility of the method with mechanical models: a fast vibroacoustic method should be developed in order to take into account the distribution of magnetic forces in the slots. The extension to outer rotor permanent magnet machines is also in the scope.

## Nomenclature

### Magnetic symbols

$\mu$	Magnetic permeability (H/m)
$\mu_0$	Magnetic permeability in free space (H/m)

$\mathbf{B}$	Magnetic flux density vector (T)
$B_r, B_\theta$	Radial and tangential magnetic flux density components
$\mathbf{H}$	Magnetic field vector (A/m)
$H_r, H_\theta$	Radial and tangential magnetic field components
$\mathbf{T}_m$	Magnetic stress tensor ( $A^2H/m^3$ )
$\mathbf{P}$	Magnetic surface force density ( $N/m^2$ )
$P_r, P_\theta$	Radial and tangential polar components of $\mathbf{P}$ ( $N/m^2$ )
$\mathbf{F}_m$	Magnetic force (N)
$S_n$	Self-transfer coefficient for AGSF
$C_n$	Cross-transfer coefficient for AGSF

### Mathematical symbols

$\hat{X}$	Complex Fourier transform of a field $X$
$\otimes$	Convolution product
$\mathbb{R}$	Space of real numbers
$\mathbb{N}$	Space of natural numbers
$\mathbb{C}$	Space of complex numbers
$j$	Imaginary number
$u_s$	Projection of a $\mathbf{u}$ vector onto the $s$ direction
$\int_\Gamma$	Integral on a domain $\Gamma$
$\nabla \cdot \mathbf{u}$	Divergence operator applied to a vector/tensor $\mathbf{u}$

## Abbreviations

AGSF	air-gap surface force
EVS	electromagnetic vibration synthesis
FEA	finite element analysis
FRF	frequency response function
MST	Maxwell stress tensor
SCIM	squirrel-cage induction machine
SPMSM	surface permanent magnet synchronous machine
VWP	virtual work principle

## References

- [1] Melcher JR. Continuum electromechanics. Cambridge, MA: MIT Press; 1981.
- [2] Abdel-Razek A, Coulomb J, Feliachi M, Sabonnadiere J. The calculation of electromagnetic torque in saturated electric machines within combined numerical and analytical solutions of the field equations. *IEEE Trans Magn.* 1981;17(6):3250–2.
- [3] Mizia J, Adamiak K, Eastham AR, Dawson GE. Finite element force calculation: comparison of methods for electric machines. *IEEE Trans Magn.* 1988;24(1):447–50.
- [4] Jang G, Yoon J, Park N, Jang S. Torque and unbalanced magnetic force in a rotational unsymmetric brushless DC motors. *IEEE Trans Magn.* 1996;32(5):5157–9.
- [5] Meessen KJ, Paulides JJH, Lomonova EA. Force calculations in 3-D cylindrical structures using fourier analysis and the maxwell stress tensor. *IEEE Trans Magn.* 2013 Jan;49(1):536–45.
- [6] Robinson FNH. Macroscopic electromagnetism. Oxford: Pergamon; 1973.
- [7] Rosensweig RE. Ferrohydrodynamics. Cambridge: Cambridge University Press; 1985.
- [8] Henrotte F, Hameyer K. Computation of electromagnetic force densities: Maxwell stress tensor vs. virtual work principle. *J Comput Appl Math.* 2004;168(1–2):235–43.
- [9] Coulomb JL, Meunier G. Finite element implementation of virtual work principal for magnetic or electric force and torque computation. *IEEE Trans Magn.* 1984 Sep;20(5):1894–6.
- [10] Henrotte F, Felden M, van der Giet M, Hameyer K. Electromagnetic force computation with the eggshell method. In: Proc. 14th International IGTE Symposium. 2010.
- [11] Sathyan S, Belahcen A, Kataja J, Henrotte F, Benabou A, Le Menach Y, et al. Computation of magnetic forces using degenerated air-gap element. *IEEE Trans Magn.* 2017 Jun;53(6):1–4.
- [12] Gieras JF, Wang C, Lai Taylor JCS. Noise of polyphase electric motors. Francis, Boca Raton, FL, USA: CRC Press; 2005.
- [13] Yu S, Tang R. Electromagnetic and mechanical characterizations of noise and vibration in permanent magnet synchronous machines. *IEEE Trans Magn.* 2006 apr;42(4):1335–8.
- [14] Saito A, Kuroishi M, Nakai H. Vibration prediction method of electric machines by using experimental transfer function and magnetostatic finite element analysis. *J Phys Conf Ser.* 2016;744(1):012088.
- [15] Boesing M, Callan-Bartkiw B, Kotter P, Zirn O, Berkemer J, Wegener K. Noise-vibration-harshness simulation of ultralight vehicle traction drives based on a universal modelling approach. 8th Int Conf PEMD 2 IET. 2016;6(1):6.
- [16] Chen X, Deng Z, Hu J, Deng T. An analytical model of unbalanced magnetic pull for PMSM used in electric vehicle: numerical and experimental validation. *IJAEM.* 2017;54(4):583–96.
- [17] Xu X, Han Q, Chu F. Review of electromagnetic vibration in electrical machines. *Energies.* 2018;11(7):1779.
- [18] Verma S, Balan A. Determination of radial-forces in relation to noise and vibration problems of squirrel-cage induction motors. *IEEE Trans Energy Convers.* 1994;9(2):404–12.
- [19] Kiyomarsi A, Zadeh MRH. A new analytical technique for analysis of the rotor eccentricity in rotating electrical machines. *IJAEM.* 2009;30(1–2):83–93.
- [20] Le Besnerais J, Lanfranchi V, Hecquet M, Friedrich G. Permeance computation for determination of induction motor acoustic noise. *Prz Elektrotech.* 2010;86(5):91–4.
- [21] Souron Q, Le Besnerais J, Hecquet M. Analysis of electromagnetically-induced vibrations of electrical machines based on spatiogram technique. *IJAEM.* 2016;51(s1):S23–32.
- [22] Azeem M, Humza M, Kim B. Analytical investigation of air-gap flux density distribution of a PM vernier motor. *IJAEM.* 2019;59(3):943–9.
- [23] Lubin T, Mezani S, Rezzoug A. Exact analytical method for magnetic field computation in the air gap of cylindrical electrical machines considering slotting effects. *IEEE Trans Magn.* 2010;46(4):1092–9.
- [24] Boughrara K, Takorabet N, Ibtouen R, Touhami O, Dubas F. Analytical analysis of cage rotor induction motors in healthy, defective, and broken bars conditions. *IEEE Trans Magn.* 2015;51(2):8200317.
- [25] Ramakrishnan K, Curti M, Zarko D, Mastinu G, Paulides JJ, Lomonova EA. Comparative analysis of various methods for modelling surface permanent magnet machines. *IET Electr Power Appl.* 2017;11(4):540–7.
- [26] Cassoret B, Corton R, Roger D, Brudny JF. Magnetic noise reduction of induction machines. *IEEE Trans Power Electron.* 2003;18(2):570–9.
- [27] Boisson J, Louf F, Ojeda J, Mininger X, Gabsi M. Analytical approach for mechanical resonance frequencies of high-speed machines. *IEEE Trans Ind Electron.* 2014;61(6):3081–8.
- [28] Boesing M, Schoenen T, Kasper KA, De, Doncker RW. Vibration synthesis for electrical machines based on force response superposition. *IEEE Trans Magn.* 2010 Aug;46(8):2986–9.
- [29] Boesing M, De Doncker RW. Exploring a vibration synthesis process for the acoustic characterization of electric drives. *IEEE Trans Ind Appl.* 2012;48(1):70–8.
- [30] Liang W. The investigation of electromagnetic radial force and associated vibration in permanent magnet synchronous machines. PhD Thesis. Cranfield: Cranfield University; 2017.
- [31] Fang H, Li D, Qu R, Yan P. Modulation effect of slotted structure on vibration response in electrical machines. *IEEE Trans Ind Electron.* 2019 April;66(4):2998–3007.
- [32] Pile R, Devillers E, Le Besnerais J. Comparison of main magnetic force computation methods for noise and vibration

- assessment in lectrical Machines. *IEEE Trans Magn.* 2018 Jul;54(7):1–13.
- [33] Hallal J, Druésne F, Lanfranchi V. Study of electromagnetic forces computation methods for machine vibration estimation. ISEF. Ohrid, Macedonia: Sept; 2013. p. 12–14.
- [34] Pile R, Parent G, Devillers E, Henneron T, Le Menach Y, Le Besnerais J, et al. Application limits of the airgap Maxwell tensor. In: CEFC 2018. 2018.
- [35] Meessen K, Paulides J, Lomonova E. Force calculations in 3-D cylindrical structures using Fourier analysis and the Maxwell stress tensor. *IEEE Trans Magn.* 2013;49(1):536–45.
- [36] Bjørk R, Smith A, Bahl CRH. Analysis of the magnetic field, force, and torque for two-dimensional Halbach cylinders. *J Magn Magn Mater.* 2010;322(1):133–41.
- [37] Pile R, Le Menach Y, Le Besnerais J, Parent G. Study of the combined effects of the air-gap transfer for Maxwell tensor and the tooth mechanical modulation in electrical machines. *IEEE Trans Magn.* 2020;56(1):1–4.
- [38] Green G. An essay on the application of mathematical analysis to the theories of electricity and magnetism. Nottingham: Printed for the author, by T. Wheelhouse; 1828.
- [39] Li M, Lowther DA. Local electromagnetic force computation in the presence of numerical field errors. *IEEE Trans Magn.* 2009 March;45(3):1344–7.
- [40] Bossavit A. Virtual power principle and Maxwell's tensor: which comes first. *COMPEL.* 2011;30(6):1804–14.
- [41] Meeker D. FEMM 4.2. User's Manual. 2015.
- [42] Garvey SD, Le Flem GD. Tangential forces matter. 9th IEMDC. 1999;468:174–8.
- [43] Roivainen J. Unit-wave response-based modeling of electro-mechanical noise and vibration of electrical machines. PhD Thesis. Helsinki: Helsinki University of Technology; 2009.
- [44] Souron Q, Le Besnerais J, Hecquet M. Analysis of electromagnetically-induced vibrations of electrical machines based on spatiogram technique. *IJAEM.* 2016 Apr;51(s1):S23–32.
- [45] Le Besnerais J. Reduction of magnetic noise in PWM supplied induction machines: low-noise design rules and multi-objective optimisation. France: Ecole Centrale de Lille; 2008.
- [46] Zhu ZQ, Xia ZP, Wu LJ, Jewell GW. Analytical modeling and finite-element computation of radial vibration force in fractional-slot permanent-magnet brushless machines. *IEEE Trans Ind Appl.* 2010 Sep;46(5):1908–18.
- [47] Lan H, Zou J, Xu Y, Liu M. Effect of local tangential force on vibration performance in fractional-slot concentrated winding permanent magnet synchronous machines. *IEEE Trans Energy Convers.* 2018;34:1082–93.
- [48] Hamiti T, Lubin T, Baghli L, Rezzoug A. Modeling of a synchronous reluctance machine accounting for space harmonics in view of torque ripple minimization. *Math Comput Simul.* 2010;81(2):354–66.
- [49] Lubin T, Mezani S, Rezzoug A. Simple analytical expressions for the force and torque of axial magnetic couplings. *IEEE Trans Energy Convers.* 2012;27(2):536–46.
- [50] Malé G, Lubin T, Mezani S, Lévêque J. Analytical calculation of the flux density distribution in a superconducting reluctance machine with HTS bulks rotor. *Math Comput Simul.* 2013;90:230–43.
- [51] Landau LD, Lifshitz E. The classical theory of fields. In: Course of theoretical physics, vol. 2. Pergamon Press; 1975.
- [52] Lee KS, DeBortoli MJ, Lee MJ, Salon SJ. Coupling finite elements and analytical solution in the airgap of electric machines. *IEEE Trans Magn.* 1991;27(5):3955–7.
- [53] Ren Z. Comparison of different force calculation methods in 3D finite element modelling. *IEEE Trans Magn.* 1994;30(5):3471–4.
- [54] Parent G, Dular P, Ducreux JP, Piriou F. Using a galerkin projection method for coupled problems. *IEEE Trans Magn.* 2008 Jun;44(6):830–3.
- [55] Le Besnerais J. Fast prediction of variable-speed acoustic noise due to magnetic forces in electrical machines. ICEM. Lausanne: IEEE; 2016; 2016. p. 2259–65.